

Submitted to The Astrophysical Journal

## Broadband Observations of the Afterglow of GRB 000926: Observing the Effect of Inverse Compton Scattering and Evidence for a High-Density Environment

F. A. Harrison<sup>1</sup>, S. A. Yost<sup>1</sup>, R. Sari<sup>2</sup>, E. Berger<sup>1</sup>, T. J. Galama<sup>1</sup>, J. Holtzman<sup>3</sup>, T. Axelrod<sup>5</sup>, J. S. Bloom<sup>1</sup>, R. Chevalier<sup>6</sup>, E. Costa<sup>7</sup>, A. Diercks<sup>1</sup>, S. G. Djorgovski<sup>1</sup>, D. A. Frail<sup>4</sup>, F. Frontera<sup>7</sup>, K. Hurley<sup>8</sup>, S. R. Kulkarni<sup>1</sup>, P. McCarthy<sup>9</sup>, L. Piro<sup>7</sup>, G. G. Pooley<sup>10</sup>, P. A. Price<sup>1</sup>, D. Reichart<sup>1</sup>, G. R. Ricker<sup>11</sup>, D. Shepherd<sup>4</sup>, B. Schmidt<sup>5</sup>, F. Walter<sup>1</sup>, C. Wheeler<sup>12</sup>

### ABSTRACT

GRB 000926 has one of the best-studied afterglows to-date, with multiple X-ray observations, as well as extensive multi-frequency optical and radio coverage. Broadband afterglow observations, spanning from X-ray to radio frequencies, provide a probe of the density structure of the circumburst medium, as well as of the ejecta energetics, geometry, and the physical parameters of the relativistic blastwave resulting from the explosion. We present an analysis of *Chandra X-ray Observatory* observations of this event, along with *Hubble Space Telescope* and radio monitoring. We combine these data with ground-based optical and IR observations and fit the synthesized afterglow lightcurve using models where collimated ejecta expand into a surrounding medium. We find that we can explain the broadband lightcurve with reasonable physical parameters only if the cooling is dominated by inverse Compton scattering. Excess X-ray emission in the broadband spectrum indicates that we are directly observing a contribution from inverse Compton scattering. It is the first time this has been observed in a GRB afterglow, and it implies that the GRB exploded in a reasonably dense ( $n \sim 30 \text{ cm}^{-3}$ ) medium, consistent with a diffuse interstellar cloud environment.

---

<sup>1</sup>Division of Physics, Mathematics and Astronomy, 105-24, California Institute of Technology, Pasadena, CA, 91125.

<sup>2</sup>Theoretical Astrophysics 130-33, California Institute of Technology, Pasadena, CA, 91125.

<sup>3</sup>Department of Astronomy, New Mexico State University, Box 30001, Department 4500, Las Cruces, NM, 88003-8001.

<sup>4</sup>National Radio Astronomy Observatory, P.O. Box O, Socorro, NM, 87801.

<sup>5</sup>Research School of Astronomy & Astrophysics, Mount Stromlo Observatory, Cotter Road, Weston, ACT, 2611, Australia.

<sup>6</sup>Department of Astronomy, University of Virginia, P.O. Box 3818, Charlottesville, VA 22903

<sup>7</sup>Istituto Astrofisica Spaziale, Consiglio Nazionale delle Ricerche, Via Fosso del Cavaliere 100, 00133 Rome, Italy.

<sup>8</sup>University of California Space Sciences Laboratory, Berkeley, CA, 94720.

<sup>9</sup>Infrared Processing and Analysis Center 100-22, California Institute of Technology, Pasadena, CA, 91125.

<sup>10</sup>Mullard Radio Astronomy Observatory, Cavendish Laboratory, Madingley Road, Cambridge CB3 0HE, England UK

<sup>11</sup>Center for Space Research, MIT, Cambridge, MA.

<sup>12</sup>Department of Astronomy, University of Texas, Austin, Texas, USA

## 1. Introduction

Broadband observations of gamma-ray burst afterglows can in principle be used to constrain fundamental physical parameters of the explosion. In the fireball model, a relativistic blast wave expands into the surrounding medium, its hydrodynamical evolution being strongly influenced by the density structure of the medium as well as by the energy content and geometry (in particular collimation) of the ejecta. The temporal behavior of the afterglow emission which arises from the shocked gas depends on the shock evolution, and the partition of energy between the magnetic field and relativistic electrons, and can therefore probe these physical parameters given data of sufficient quality.

In this paper, we report the synthesized results from our multi-frequency followup campaign on the relatively bright GRB 000926. This campaign was aimed at studying the evolution of the afterglow to constrain the model parameters described above. Price et al. (2001) have reported the results from our multi-band (*BVRI*) optical monitoring. We combine these data with 4 epochs taken with the *Hubble Space Telescope* WFPC2, with *Chandra X-ray Observatory* (CXO) target of opportunity (TOO) observations, and with multi-frequency radio monitoring from the Very Large Array (VLA)<sup>13</sup>, the Ryle Telescope, and the Owens Valley Radio Observatory. We interpret the resulting broadband lightcurve in the context of a theoretical afterglow model.

## 2. Observations and Data Reduction

The Interplanetary Network discovered GRB 000926 on 2000 Sep 26.993 UT (Hurley et al. 2000). The afterglow of this 25 s long event was identified less than a day later (Gorosabel et al. 2000; Dall et al. 2000). The redshift, measured from optical absorption features, is  $2.0369 \pm 0.0007$  (Fynbo et al. 2000; Castro et al. 2000). The afterglow was well-monitored in the optical (Price et al. 2001; Fynbo et al. 2001), detected in the IR (DiPaola et al. 2000; Fynbo et al. 2001). Here we describe *Hubble Space Telescope* (*HST*), *Chandra X-ray Observatory* (CXO) and radio observations.

### 2.1. HST Observations

As part of an *HST* cycle 9 program we observed GRB 000926 at four epochs with the Wide Field Planetary Camera 2 (WFPC2), with the OT placed on WFPC CCD#3. In the first three epochs we observed at three passbands corresponding to the F450W, F606W, and F814W filters, and in the final epoch we used only the F606W and F814W filters. These observations took place between Oct 7.25 (10.26 days after the GRB) and Dec 16.9 (81.9 days after).

Table 1 shows a log of the HST observations, along with the magnitude derived for each filter for the 2-pixel radius region surrounding the OT. We determined the aperture correction using a 2 – 5 pixel radius, and we quote the corresponding 5 pixel radius magnitude. We calibrated the zeropoints, and converted the WFPC2 filters to Johnson Cousins magnitudes using the color transformations from Holtzman et al. (1995). We estimate the associated calibration uncertainty to be about 0.10 magnitude in *B*, *V*, *R* and *I* bands. We tied the WFPC2 calibration to the ground-based data of Price et al. (2001) using their tertiary

---

<sup>13</sup>The NRAO is a facility of the National Science Foundation operated under cooperative agreement by Associated Universities, Inc. NRAO operated the VLA

Table 1. WFPC2 HST observations of the GRB 000926 optical afterglow.

Date (2000, UT)	Filter	Exposure time (sec)	Magnitude
Oct 7.25	F450	2x1100 (1 orbit)	24.98 $\pm$ 0.07
Oct 7.35	F606	4x1100 (2 orbits)	24.54 $\pm$ 0.03
Oct 7.49	F814	4x1100 (2 orbits)	23.89 $\pm$ 0.03
Oct 16.08	F450	2x1100 (1 orbit)	25.82 $\pm$ 0.14
Oct 16.18	F606	4x1100 (2 orbits)	24.27 $\pm$ 0.03
Oct 16.32	F814	4x1100 (2 orbits)	24.87 $\pm$ 0.05
Oct 25.05	F450	2x1100 (1 orbit)	25.59 $\pm$ 0.12
Oct 25.21	F606	4x1100 (2 orbits)	25.45 $\pm$ 0.03
Oct 25.35	F814	4x1100 (2 orbits)	24.96 $\pm$ 0.05
Dec 16.02	F606	6x1000 (3 orbits)	25.58 $\pm$ 0.03
Dec 16.90	F814	4x1100 (2 orbits)	25.24 $\pm$ 0.07

Table 2. OT Magnitudes Measured by HST

T (Days after GRB)	Frequency (GHz)	Flux $\pm\sigma$ ( $\mu$ Jy)
10.3570	$6.871 \times 10^{14}$ (B)	0.233 $\pm$ 0.039
19.1870	$6.871 \times 10^{14}$ (B)	-0.011 $\pm$ 0.037
28.2170	$6.871 \times 10^{14}$ (B)	0.057 $\pm$ 0.039
10.3570	$5.499 \times 10^{14}$ (V)	0.257 $\pm$ 0.023
19.1870	$5.499 \times 10^{14}$ (V)	0.056 $\pm$ 0.019
28.2170	$5.499 \times 10^{14}$ (V)	0.008 $\pm$ 0.018
80.4670	$5.499 \times 10^{14}$ (V)	-0.004 $\pm$ 0.018
10.3570	$4.673 \times 10^{14}$ (R)	0.398 $\pm$ 0.029
19.1870	$4.673 \times 10^{14}$ (R)	0.072 $\pm$ 0.023
28.2170	$4.673 \times 10^{14}$ (R)	0.034 $\pm$ 0.022
80.4670	$4.673 \times 10^{14}$ (R)	-0.004 $\pm$ 0.021
10.3570	$3.806 \times 10^{14}$ (I)	0.525 $\pm$ 0.029
19.1870	$3.806 \times 10^{14}$ (I)	0.075 $\pm$ 0.022
28.2170	$3.806 \times 10^{14}$ (I)	0.053 $\pm$ 0.021
80.4670	$3.806 \times 10^{14}$ (I)	-0.012 $\pm$ 0.024

star at position RA  $12^h 04^m 11^s.75$  DEC  $+51^\circ 46' 56''$ .1 (J2000). The magnitudes we derive for this star agree with those obtained by Price et al. (2001) to within 0.10 mag in  $B$ ,  $V$ , and  $R$ , and to within 0.20 mag in  $I$ . Galama et al. (2001) provide further details on the image reduction and magnitude calibration.

From flattening in the late-time ( $t \gtrsim 10$  days) optical lightcurve we infer that the HST data are contaminated by a contribution from the host galaxy. We do not actually resolve the host in our HST images, and we observe flattening even with our small ( $0.14''$ ) extraction radius. This implies that the host itself is compact, or that the constant emission is from a bright knot or filament associated with the host. Future HST observations scheduled for April 2001 may resolve this feature, and we will present these results elsewhere. To determine the flux from the OT we subtract this constant contribution.

To derive the magnitude for the constant term, we fit the ground-based optical lightcurve from Price *et al.* (2001) combined with our HST data to a decaying function with a constant added:

$$F(t, \nu) = F_0 \nu^\beta \left( (t/t_*)^{-\alpha_1 s} + (t/t_*)^{-\alpha_2 s} \right)^{-1/s} + F_{\text{host}}(\nu). \quad (1)$$

The decaying function, taken from Beuermann et al. (1999), has no physical significance, but provides a simple and general parametric description of the data. Here  $\alpha_1$  and  $\alpha_2$  are the early and late time asymptotic temporal slopes respectively,  $t_*$  is the time of the temporal slope break,  $s$  is a parameter that determines the sharpness of the transition, and  $\beta$  is the spectral slope. From the combined ground-based and HST data we derive  $\alpha_1 = 1.49$ ,  $\alpha_2 = 2.38$ ,  $t_* = 1.8$  days,  $\beta = -1.55$ . The best-fit value for the constant is  $F_{\text{host}}(B) = 25.77 \pm 0.14$ ,  $F_{\text{host}}(V) = 25.60 \pm 0.1$ ,  $F_{\text{host}}(R) = 25.38 \pm 0.1$ ,  $F_{\text{host}}(I) = 25.12 \pm 0.10$ . We note that our fit values are similar to those derived by Price et al. (2001), but the late-time, high-resolution HST data allow us to determine the flux from the compact region near the OT.

We derive the OT magnitudes by subtracting the constant term,  $F_{\text{host}}$ , given above from each band, correcting for the foreground Galactic extinction of  $E_{B-V} = 0.0235$  mag (Schlegel, Finkbeiner & Davis 1998). Table 1 contains the resulting dereddened, host-subtracted OT flux values converted to  $\mu\text{Jy}$ . The measurement errors include a contribution ( $1-\sigma$ ) of 0.026(B), 0.016 (V), 0.018 (R), 0.020 (I)  $\mu\text{Jy}$  added in quadrature to the statistical and systematic calibration errors to reflect the uncertainty in the constant host term derived from the fit.

Table 3. X-ray Transient Flux

T (Days after GRB)	Frequency (GHz)	Flux $\pm\sigma$ ( $\mu\text{Jy} \times 10^2$ )
2.7700	$1.14 \times 10^{17}$	$3.98 \pm 0.594$
13.477	$1.14 \times 10^{17}$	$0.156 \pm 0.035$
2.2780	$7.5 \times 10^{17}$	$1.78 \pm 0.621$
2.7700	$7.5 \times 10^{17}$	$0.684 \pm 0.070$
13.477	$7.5 \times 10^{17}$	$0.029 \pm 0.016$

## 2.2. CXO Observations

The *BeppoSAX* Medium Energy Concentrating Spectrometer (MECS) instrument (sensitive from 1.6 – 10 keV) discovered the X-ray afterglow of GRB 000926 in an observation made on Sep 29.03 – 29.52 (Piro et al. 2000). Garmire et al. (2000) observed the source for 10 ksec as part of a Cycle 1 CXO program using the ACIS S3 backside-illuminated chip on Sep 29.674 – 29.851 (referred to here as CXO-P1). Supporting our HST cycle 9 program, CXO again observed GRB 000926 in a 33-ksec long TOO taken Oct 10.176–10.76 UT (CXO-P2), also with the transient placed on the ACIS S3 backside-illuminated chip. The afterglow was clearly detected in each of these observations. The transient was not detected in the *BeppoSAX* Low Energy Concentrating Spectrometer (co-aligned with the MECS, and sensitive in the 0.1 – 10 keV band), however the effective exposure time was only 5 ksec. Piro et al. (2001) present a detailed spectral analysis of the X-ray data, including combined fits to all pointings.

We analyzed the data from CXO-P1 and CXO-P2 using software provided by the *Chandra* X-ray Observatory Center (CXC) to filter the events, extract source counts and subtract background. For the latter we used an annular region surrounding the source. We fit the two *Chandra* pointings separately using a powerlaw model plus absorption. The best fit photon spectral index for the CXO-P1 data is  $\alpha = 1.9 \pm 0.21$  and for CXO-P2 is  $\alpha = 2.23 \pm 0.34$ , with best-fit hydrogen column depth  $N_H = (4.8 \pm 3) \times 10^{20} \text{ cm}^{-2}$  (CXO-P1) and  $N_H = (3.0 \pm 2.5) \times 10^{20} \text{ cm}^{-2}$  (CXO-P2). We find no evidence for additional absorption in the X-ray spectrum at the redshift of the host ( $z = 2.04$ ). This is consistent with the host  $A(V)$  of 0.1 mag derived from model fits to the optical data (see below), if we adopt typical dust to gas ratios. For an LMC-like extinction curve, for example, this  $A(V)$  corresponds to column depth of  $N_H = 2 \times 10^{20} \text{ cm}^{-2}$  for a host at  $z = 2.04$ . Given the host redshift, such a low column is not detectable in the X-ray spectrum, and so no correction for absorption in the GRB host is necessary.

The detection statistics in the X-ray are limited, so for the purposes of our modeling we divided the energy range into soft (0.2 – 1.5 keV) and hard (1.5 – 8 keV) bands. We converted counts to flux using exposure maps weighted in energy using a photon powerlaw spectral index of  $\alpha = 2$  and  $N_H = 2.7 \times 10^{20} \text{ cm}^{-2}$ , corresponding to the value for our own Galaxy, as determined by W3nH<sup>14</sup>. We adopt this value since it is consistent with that derived from our spectral modeling, and we find no significant evidence for additional absorption in the host. For the *SAX* observation, we used the best fit spectral model to determine the hard band flux (the MECS response does not allow a soft-band flux to be determined).

---

<sup>14</sup>W3nH is available at <http://heasarc.gsfc.nasa.gov>.

Table 4. X-ray Afterglow of GRB000926

Pointing	Epoch (2000, UT)	Band (keV)	Flux $\pm \sigma$ (erg/cm <sup>2</sup> /s $\times 10^{13}$ )
SAX	Sep. 29.03 – 29.53	1.5 – 8	$2.23 \pm 0.77$
CXO - P1	Sep.29.674 – 29.851	0.2 – 1.5	$0.614 \pm 0.063$
CXO - P1	Sep.29.674 – 29.851	1.5 – 8	$0.939 \pm 0.14$
CXO - P2	Oct.10.176 – 10.760	0.2 – 1.5	$0.0263 \pm 0.008$
CXO - P2	Oct.10.176 – 10.760	1.5 – 8	$0.0364 \pm 0.019$

Table 3 shows the flux values, not corrected for Galactic absorption, for the three observations. To determine the center energy for the band, we took the mean, weighted using a photon index of  $\alpha = 2$ . We determined flux errors by adding in quadrature the statistical error and the error due to the uncertainty in spectral slope. Since the flux is decaying during each observation interval, we weight the time of the observation by  $t^{-2}$  and average to determine the mean epoch. Table 4 lists the center frequencies and flux values for the X-ray transient (converted to  $\mu\text{Jy}$ ), where we have corrected for Galactic absorption.

### 2.3. Radio Observations

We obtained radio observations at frequencies from 1.43 to 100 GHz at a number of facilities: the Owens Valley Radio Observatory Interferometer (OVRO), the Ryle Telescope, and the VLA. Table 5 summarizes these observations, organized by frequency. The 98.48 GHz data were taken at OVRO, the 15 GHz data at Ryle, and all other frequencies were observed using the VLA. In performing the observations, reducing the data and deriving flux errors we adopted the methodology described in detail in Kulkarni et al. (1999), Frail et al. (2000), and Berger et al. (2000). For the OVRO observations, we used the quasar 1726+455 for phase calibration and Uranus for absolute flux calibration.

## 3. Afterglow Model

To interpret the broadband lightcurve we employ a model for the emission from the relativistic shock (resulting from the GRB explosion) as it expands into the surrounding medium. Our modeling is quite comprehensive. It allows for either a constant density medium (which we refer to as ISM), or for a density depending on radius as  $\rho = Ar^{-2}$  referred to as the wind model, since this profile would be produced by a stellar progenitor's wind (Chevalier & Li 1999). We also allow for either isotropic or collimated ejecta, and we fit for extinction in the host galaxy. We include the effects of inverse Compton scattering on the evolution of the synchrotron spectrum, as well as the contribution of IC emission to the observed spectrum. IC scattering is not included in most models used to fit GRB afterglows, but if the ambient medium is of sufficiently high density, it becomes an important effect. Compton emission can dominate the total afterglow cooling rate for months after the event, and can even be directly observed in the X-ray (Panaitescu & Kumar 2000; Sari & Esin 2001).

We calculate the shock emission at a given time and frequency from a number of fundamental parameters: the initial isotropic-equivalent energy,  $E$  in the shock, the electron powerlaw slope,  $p$ , the electron and magnetic field energy fractions,  $\epsilon_e$  and  $\epsilon_B$ , and the density of the circumburst medium. We employ the equations given by Sari, Piran & Narayan (1998) and Granot, Piran & Sari (1999a,b) to determine the evolution of the synchrotron spectrum for the constant density medium, and the equations given by Chevalier & Li (1999, 2000) for the wind model. We include the effect of inverse Compton scattering using the treatment given by Sari & Esin (2001). We calculate the time at which collimation becomes evident ( $\theta = 1/\Gamma$ , where  $\Gamma$  is the Lorentz factor of the ejecta) and the subsequent spectral evolution using Sari, Piran & Halpern (1999). For the host extinction we use the parameterization of  $A(V)$  of Cardelli et. al. (1989) and Fitzpatrick & Massa (1998), joined using the formula from Rechard (1999) in the rest-frame optical/UV, and absorption cross-sections given by Morrison & McCammon (1983) in the rest-frame X-ray. We consider both LMC or SMC-like extinction laws. To fit the broadband lightcurve we vary the fundamental parameters, iterating to minimize  $\chi^2$ .

Table 5. Radio Observations of GRB000926

Epoch (2000, UT)	Frequency (GHz)	Flux $\pm\sigma$ ( $\mu\text{Jy}$ )
Sep 29.708	98.48	3410 $\pm$ 1020
Oct 1.708	98.48	1890 $\pm$ 750
Oct 4.186	22.5	1415 $\pm$ 185
Oct 5.216	22.5	1320 $\pm$ 240
Oct 16.721	22.5	480 $\pm$ 230
Sep 28.81	15.0	490 $\pm$ 230
Sep 30.91	15.0	-320 $\pm$ 520
Oct 1.69	15.0	820 $\pm$ 390
Oct 5.751	15.0	460 $\pm$ 330
Oct 11.751	15.0	340 $\pm$ 220
Sep 28.17	8.46	666 $\pm$ 60
Sep 28.97	8.46	150 $\pm$ 55
Sep 29.726	8.46	368 $\pm$ 26
Oct 4.186	8.46	440 $\pm$ 34
Oct 5.216	8.46	566 $\pm$ 34
Oct 7.771	8.46	564 $\pm$ 76
Oct 8.291	8.46	143 $\pm$ 77
Oct 10.281	8.46	242 $\pm$ 130
Oct 12.771	8.46	644 $\pm$ 126
Oct 15.681	8.46	379 $\pm$ 36
Oct 23.161	8.46	277 $\pm$ 34
Oct 27.131	8.46	170 $\pm$ 79
Oct 30.181	8.46	192 $\pm$ 41
Nov 26.64	8.46	143 $\pm$ 35
Dec 18.95	8.46	160 $\pm$ 21
Jan 29.44	8.46	10 $\pm$ 40
Feb 9.73	8.46	71 $\pm$ 12
Sep 28.17	4.86	90 $\pm$ 67
Sep 28.97	4.86	100 $\pm$ 45
Sep 29.726	4.86	280 $\pm$ 29
Oct 4.186	4.86	248 $\pm$ 30
Oct 7.741	4.86	395 $\pm$ 61
Oct 8.701	4.86	370 $\pm$ 70
Oct 30.201	4.86	210 $\pm$ 33
Nov 18.03	4.86	131 $\pm$ 45
Jan 6.53	4.86	62 $\pm$ 42
Feb 2.47	4.86	54 $\pm$ 41
Feb 19.28	4.86	126 $\pm$ 23
Dec 16.58	1.43	96 $\pm$ 46

At any given time the synchrotron emission, which dominates at most energies, has a spectrum characterized by a number of breaks: a low-frequency roll over due to self-absorption at frequency  $\nu_a$ ; a peak at frequency  $\nu_m$  due to the peak energy in the electron distribution; and a cooling break at  $\nu_c$ , where radiative energy losses become a significant fraction of the electron energy. These breaks evolve in time as the shock evolves, producing frequency-dependent breaks in the lightcurve. For the case of collimated ejecta, the lightcurve will begin to steepen when  $\theta$  is smaller than the angle into which the emission is beamed due to relativistic effects ( $1/\Gamma$ , where  $\Gamma$  is the Lorentz factor). We use a sharp transition for this “jet break”, and employ spherical evolution laws up until the time of the break. After the jet transition we assume the ejecta expand laterally, and we employ the appropriate asymptotic formulae until the time the ejecta become non-relativistic. The transition to the non-relativistic evolution is again treated as sharp.

The inverse Compton component is also characterized by a series of spectral breaks. With the synchrotron spectrum as the photon source, Sari & Esin (2001) find that the upscattered component is characterized by three breaks at  $\nu_a^{IC} \sim 2\min(\gamma_c, \gamma_m)^2 \nu_a$ ,  $\nu_m^{IC} \sim 2\gamma_m^2 \nu_m$ ,  $\nu_c^{IC} \sim 2\gamma_c^2 \nu_c$  where  $\gamma_m$  is the characteristic Lorentz factor of the electrons emitting with peak frequency  $\nu_m$ . We adopt a spectral shape for the IC component similar to the synchrotron spectrum, but with the breaks given by the values in Sari & Esin (2001). This provides a good approximation to the IC component spectral shape except for at  $\nu < \nu_a^{IC}$ , but for our data this is not a concern (see below). Between  $\nu_m^{IC}$  and  $\nu_c^{IC}$  there is only a logarithmic correction, which we ignore.

#### 4. Fits to the Broadband GRB 000926 Lightcurve

We fit the broadband GRB 000926 lightcurve employing the afterglow model described above. In addition to the data in Tables 1 – 4, we included the ground-based optical points given in Price et.al. (2001), as well as  $J$  band data from DiPaola et al. (2000) and  $J, H, K'$  and  $K$ -band points from Fynbo et al. (2001). We converted the  $K'$  points to  $K$  using the prescription in Wainscoat & Cowie (1992). All the data are corrected for absorption in our Galaxy, and in the case of the optical data we subtracted the contribution from the host.

We considered several possible cases in fitting the data; constant density as well as a density gradient for the surrounding medium, and two cases for the IC emission. The need to consider two cases arises from the fact that for the same synchrotron emission spectrum, Sari & Esin (2001) find two possible IC solutions. These correspond to the two limits  $\eta\epsilon_e/\epsilon_B \equiv f \ll 1$ , and  $f \gg 1$ , where  $\epsilon_e$  and  $\epsilon_B$  are the fractions of the total explosion energy that go into accelerating shocked electrons and amplifying the post-shock magnetic field respectively. Here  $\eta$  is the fraction of electron energy radiated away, so describes whether cooling is dominant. If  $f \ll 1$  (low IC), the IC cooling rate is unimportant compared to that of synchrotron, whereas if  $f \gg 1$  (high IC) inverse Compton cooling dominates the total emission.

Two features are required by all the models we considered. The ejecta must be collimated in order to explain the break in the optical lightcurve at 1–2 days. In the optical, this break is roughly independent of frequency. Extinction, presumably due to the host galaxy, is required to fit the optical spectrum. The best-fit value is  $A(V) \sim 0.1$  mag for LMC-like extinction, with the magnitude being relatively insensitive to the extinction law. These two features – collimation and extinction – are therefore independent of other assumptions made in the modeling (such as the density model or IC solution). Price et al. (2001) derived similar values based on fits to the optical data alone.

The only model which represents the broadband data well is a constant density ISM with the high-IC

solution. Figures 1a and 1b show the broadband spectrum around day 2 and day 10, with the best-fit model overplotted. Figures 2, 3, and 4 show the X-ray, optical and radio lightcurves. The first column of data in Table 6 lists the physical parameters for the best fit high-IC solution. The derived parameters are all reasonable, although we note that  $\epsilon_e$  of 0.30 is only marginally consistent with the assumption of adiabatic evolution inherent to our model. While this will not alter our basic conclusions, in future work we will expand the model to include partially radiative blast waves (see Sari (1997) and Cohen, Piran & Sari (1998) for treatments of the afterglow evolution in this case). The  $\chi^2$  for the fit is 188 for 107 degrees of freedom if we include all data points. The largest contribution comes from the first 8.46 GHz data point, and from the  $I$  and  $J$ -band optical data. The 8.46 GHz point may be associated with a separate component from the reverse shock (see below), and although the model represents the slope and magnitude of the  $I$ -band data, the observations exhibit significant scatter in excess of our estimated systematic and statistical uncertainties. We have likely not properly accounted for fringing and other effects that uniquely effect these observations. If we exclude these data we obtain a good formal fit, with  $\chi^2 = 114$  for 96 degrees of freedom.

The physical parameters we derive for the high-IC ISM model (Table 6) are reasonable. We note here that the isotropic-equivalent energy in the blast wave,  $1.8 \times 10^{53}$  erg, is valid for  $t \gtrsim 1$  day. We use an adiabatic model to fit the data, which assumes the total energy is constant in time. This is accurate for  $t \gtrsim 2$  days, and we do not have any early data ( $t < 1$  day). The adiabatic assumption is therefore reasonable over the interval we are considering. At early times, however, the blast wave energy decreases with time. In particular, for the high-IC case, the shock wave radiates a significant amount of energy early on, emitted as MeV gamma-rays. Using the equations in Cohen, Piran & Sari (1998) we estimate the energy in the initial fireball to be about five times higher than that associated with the adiabatically expanding blast wave at a few days, or  $E_{\text{initial}} \sim 1 \times 10^{54}$  erg. The observed isotropic energy release in the gamma-ray burst itself was  $E_\gamma = 3 \times 10^{53}$  erg (Hurley et al. 2000). Recent theoretical work suggests the internal shock process producing the GRB should radiate less energy than the blast wave, except under extreme physical conditions (Beloborodov 2000; Kobayahi & Sari 2001). The value we derive for the fireball energy is, therefore, reasonable.

Figure 2 shows the X-ray data with both high and low-IC ISM models overplotted. Interestingly, the low-IC case under-predicts the X-ray flux by more than a factor of two. Piro et al. (2001) noted an excess in the X-ray band over the prediction of a standard synchrotron model, which they attributed to a very high density ( $n \sim 10^4 \text{ cm}^{-3}$ ) medium. This high density is inconsistent with the extinction we measure in the optical, unless most of the dust along the line of sight is destroyed by the GRB radiation. Rather, we find that the X-ray excess is due to the IC scattered component. Figure 1a shows the broadband spectrum around day 2 with the high-IC model broken into Compton-scattered and synchrotron components. The IC contribution accounts for the excess above the extrapolation of the synchrotron component. IC scattering has the additional effect of hardening the X-ray spectrum over some time intervals, compared to the prediction from synchrotron emission alone. There is only marginal evidence for this in the data; the observed X-ray spectral photon index is  $1.9 \pm 0.21$  compared with the  $p/2 + 1 = 2.2$  associated with the synchrotron component. X-ray data with higher statistical accuracy will be of interest to directly observe this spectral hardening in future events.

From Figure 2 it is evident that the approximation to the IC contribution made by assuming the same shape as the synchrotron is not an issue. As mentioned previously, the error in this approximation is only significant below  $\nu_a^{IC}$ , and for the parameters we derive the synchrotron dominates the total flux in this region by several orders of magnitude.

The low-IC ISM model is both a poor fit ( $\chi^2 = 220$  for 107 degrees of freedom, or  $\chi^2 = 169$  if outliers

are excluded), and implausible due to the unrealistic physical parameters associated with this case. Table 6 compares the best-fit values for the low-IC and high-IC ISM solutions. The low-IC magnetic field energy fraction is  $\epsilon_B = 24$ . Formally of course  $\epsilon_B > 1$  is physically impossible, however due to approximations in the model (multiplicative factors of order unity) we cannot exclude  $\epsilon_B$  of a few. However, the large value of  $\epsilon_B = 24$  exceeds what we can explain due to approximations in our theoretical treatment. Furthermore, the isotropic-equivalent energy in the blast wave of  $10^{53}$  erg for the low-IC case is smaller than the observed gamma-ray energy release. Radiative corrections are much smaller than in the high-IC case, so that the adiabatic value more closely represents the energy in the initial fireball. As pointed out above,  $E_\gamma \gtrsim E_{\text{fireball}}$  is hard to accomodate except under extreme conditions.

We also investigated a wind density profile in both high- and low-IC regimes. Neither of these cases reproduce the data as well as the high-IC ISM model. The low-IC wind solution under-predicts the X-ray flux by a factor 2.5. Further, the  $\epsilon_B$  of 174 derived for this case is unreasonably large. The high-IC wind case under-predicts the 5 GHz radio data by a factor 2 – 3, but reproduces the X-ray data reasonably well. Although it is not as good a fit, we cannot confidently rule out a high-IC wind model. Given the approximations in the theoretical treatment, confidently determining the density structure will require early-time optical or high-frequency radio data. This is because the lightcurve evolution after the jet break is similar for ISM and wind. Directly observing the cooling break evolution provides the greatest leverage, since this evolution is significantly different for wind and ISM models. Generally, this requires optical observations or high-frequency radio observations at early epochs (minutes to hours after the event).

Finally, we point out that even for our best fit (high-IC ISM) solution, the first 8 GHz data point exceeds the model’s expectation by a factor of 3.3 (7.9  $\sigma$ ). This discrepancy is worse for the alternative models. Scintillation gains this large are extremely improbable, and it is therefore likely that we are seeing evidence for an additional component due to the reverse shock emission, as was observed in early radio observations of GRB 990123 (Kulkarni et al. 1999).

## 5. Conclusions

GRB 000926 has one of the highest-quality broadband afterglow lightcurves studied to-date. We can explain all the general features using a model of a relativistic shock produced by ejecta collimated to a  $\sim 8^\circ$  opening angle. If we correct the isotropic-equivalent gamma-ray energy release for this jet angle we get  $E_\gamma = E_{\gamma,iso} \times \theta^2/2 = 3 \times 10^{51}$  erg. This is reasonably accounted for in most currently-popular progenitor models. Our observations require extinction in the host galaxy, with a corresponding hydrogen column of  $\sim 2 \times 10^{20}$  cm $^{-2}$  if the dust to gas ratio is typical of the LMC or SMC. This is consistent with the event taking place in a galactic disk.

We find that an explosion occurring in a relatively dense, spatially homogeneous medium best describes the broadband lightcurves, provided that the ratio  $\eta\epsilon_e/\epsilon_B \gg 1$ . This condition implies that Compton emission dominates the total cooling rate, and that IC scattering is potentially directly observable in the afterglow spectrum. We do, in fact, find direct evidence for an IC contribution in the X-ray band, where all models with  $\eta\epsilon_e/\epsilon_B \ll 1$  significantly under-predict the observed flux. Detecting the IC emission in the X-ray band directly implies a lower-limit on the density (Panaitescu & Kumar 2000; Sari & Esin 2001), in this case  $n \gtrsim 10$  cm $^{-3}$ , and our best fit yields  $n = 30$  cm $^{-3}$ . This value for  $n$  is higher than the average ISM density in a typical galaxy, and is consistent with a diffuse interstellar cloud, such as those commonly found in star forming regions. Combining the density with the host  $N_H$  derived from our optical observations

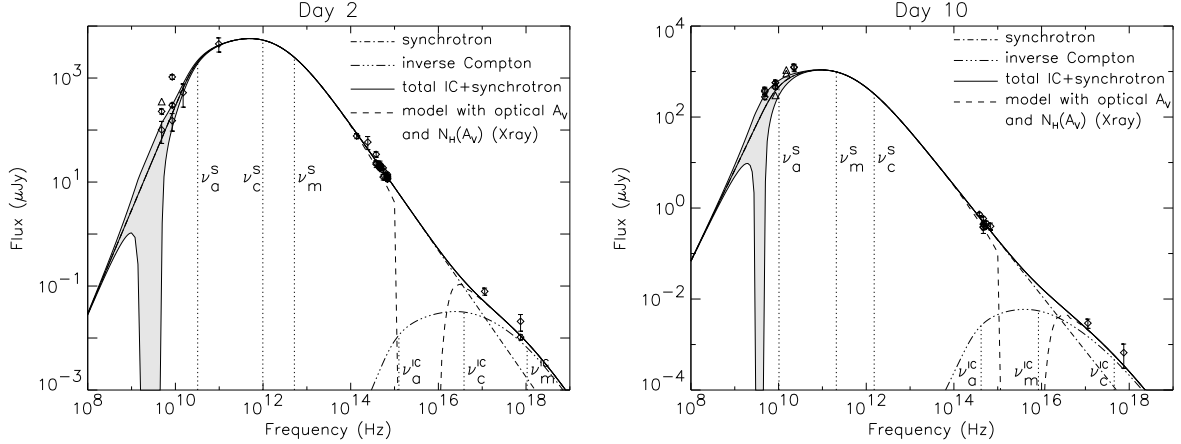


Fig. 1.— (a) The broadband spectrum of the GRB 000926 afterglow on day 2 (after the jet break). All data taken between 1 – 3 days are included, where we have used the model calculations to extrapolate the points forward or backward in time. The relative error seen in the graph therefore represents the true deviation of the observed data from the model at the exact time of the observations. The data, corrected for host extinction, are shown by diamonds, with  $1 - \sigma$  errors, the solid line is the best-fit model without host extinction, and the dashed line shows model plus extinction. The locations of the synchrotron spectral breaks  $\nu_a^s$ ,  $\nu_c^s$ , and  $\nu_m^s$  associated with self-absorption, cooling, and the maximum electron energy are indicated. We also indicate the corresponding breaks for the IC spectrum (see Sari & Esin (2001) for details). (b) The broadband spectrum of the GRB 000926 afterglow on day 10 (after the jet break).

Table 6. Fit parameters for low and high-IC ISM and Wind models.

Parameter	high-IC ISM	low-IC ISM	high-IC Wind	low-IC Wind
$\chi^2$ for 96 dof <sup>c</sup>	114	169	169	179
$\chi^2$ for 107 dof	188	220	234	231
$t_{\text{jet}}$ (days)	1.55	1.29	1.87	1.27
$t_{\text{nonrel.}}$ (days)	70	293	119	931
$E_{\text{iso}}^{\text{a}}$ ( $10^{52}$ erg)	18	9.1	110	30
$n(\text{ISM})/A_*(\text{wind})^{\text{b}}$	$27 \text{ cm}^{-3}$	$0.04 \text{ cm}^{-3}$	6.7	0.02
$p$	2.43	2.21	2.74	2.20
$\epsilon_e$ (fraction of E)	0.30	0.12	0.21	0.017
$\epsilon_B$ (fraction of E)	0.0076	24	$3.4 \times 10^{-4}$	174
$\theta_{\text{jet}}$ (rad)	0.14	0.061	0.089	0.026
host A(V)	0.12	0.18	0.06	0.18

<sup>a</sup>Isotropic equivalent energy (not corrected for collimation).

<sup>b</sup> $\rho = A_*(5 \times 10^{11})r^{-2} \text{ g cm}^{-3}$

<sup>c</sup>First 8.46 GHz and the J- and I-band points excluded as outliers

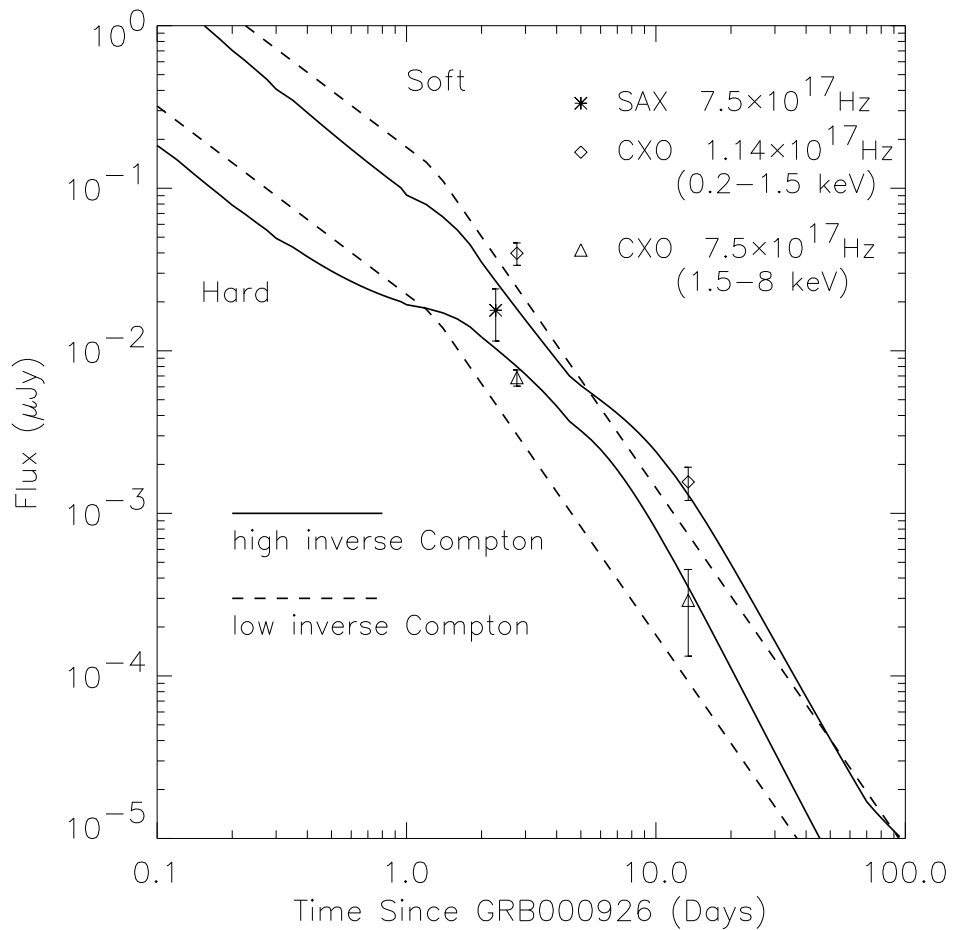


Fig. 2.— The X-ray afterglow lightcurve from *BeppoSAX* and *Chandra*. The *Chandra* data have been broken into two bands, hard (1.5 – 8 keV) and soft (0.2 – 1.5 keV), with center frequencies (weighted with a photon spectral index of  $\alpha = 2$ ) of  $7.5 \times 10^{17}$  Hz and  $1.14 \times 10^{17}$  Hz respectively. The data have been corrected for absorption in our Galaxy (column of  $N_H = 2.65 \times 10^{20}$  cm $^{-2}$ ). We also show the model calculations for both high- (solid line) and low-IC (dashed line) constant-density ISM models.

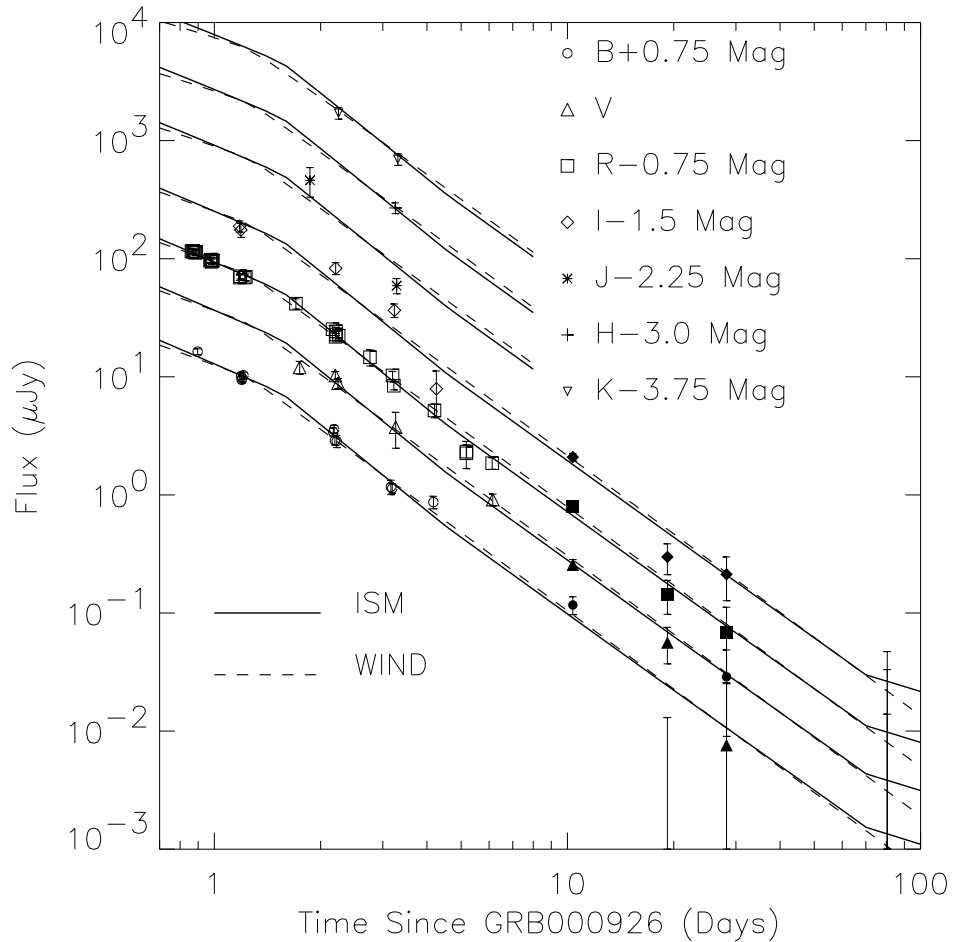


Fig. 3.— The optical/IR afterglow lightcurve in seven bands. We have subtracted the host contribution, as determined from the late-time *HST* data, and corrected for Galactic extinction. The ISM (solid lines) and best-fit wind (dashed line) models include the effect of extinction in the host galaxy, as determined by the best-fit value using an extinction curve (dust to gas ratio) like that of the LMC.

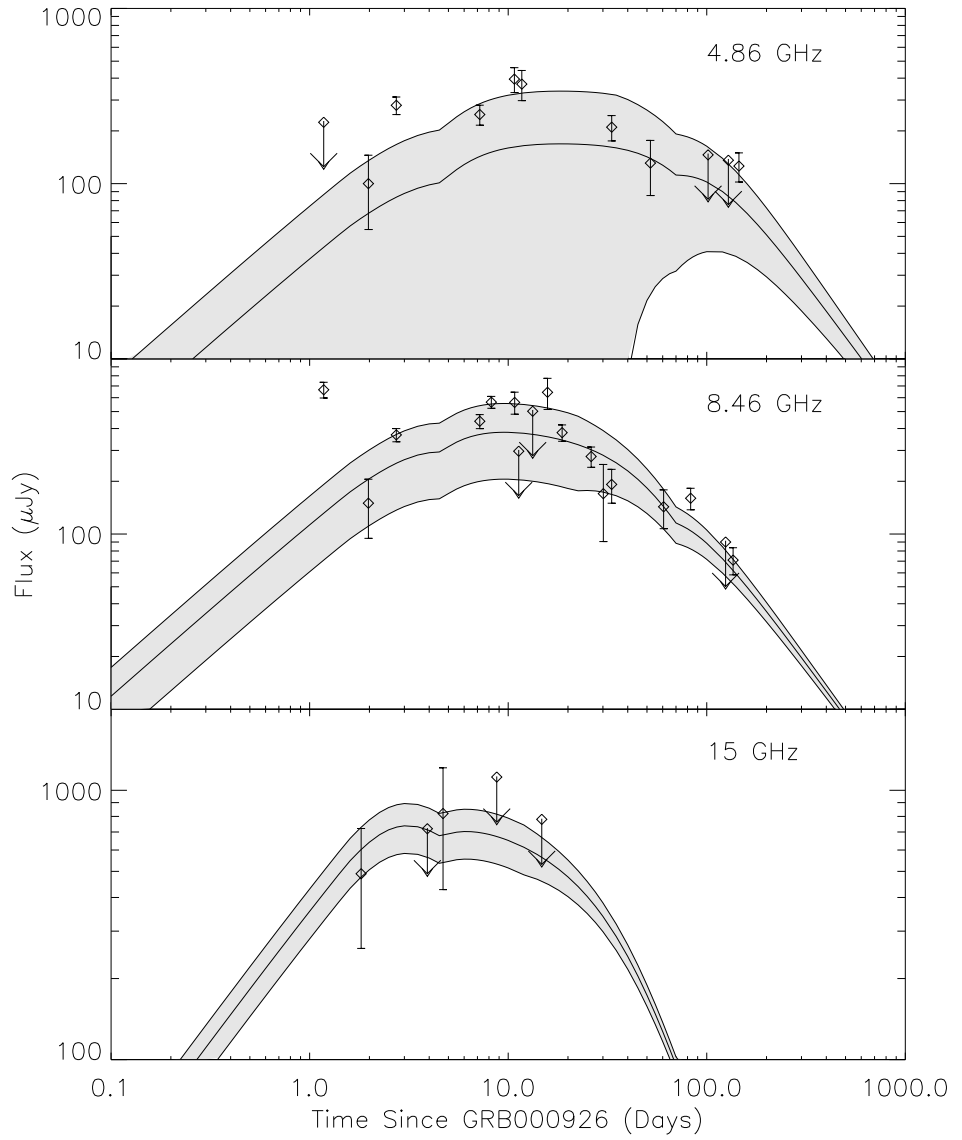


Fig. 4.— The radio lightcurve at three frequencies. The solid lines show the model calculations based on the high-IC ISM solution. The shaded regions indicate the estimated scintillation envelopes based on the calculated size of the fireball.

(again assuming typical dust to gas ratios) implies a scale size of 2 pc for the cloud.

We wish to thank Harvey Tananbaum and the CXO operations staff for facilitating the *Chandra* TOO observations. We thank Steve Beckwith and the HST operations staff for facilitating the WFPC2 observations. FAH acknowledges support from a Presidential Early Career award. SRK and SGD thank NSF for support of their ground-based GRB programs. RS is grateful for support from a NASA ATP grant. RS & TJG acknowledge support from the Sherman Fairchild Foundation.

## REFERENCES

Beloborodov, A. M. 2000, ApJ, 539, L25.

Berger, E. et al. 2000, ApJ, 545, 56.

Beuermann, K. et al. 1999, A&A, 352, L26.

Castro, S. M., Djorgovski, S. G., Kulkarni, S. R., Bloom, J. S., Galama, T. J., Harrison, F. A., and Frail, D. A. 2000, GCN notice 851.

Chevalier, R. A. and Li, Z. 2000, ApJ, 536, 195.

Chevalier, R. A. and Li, Z.-Y. 1999, ApJ, 520, L29.

Cohen, E., Piran, T., and Sari, R. 1998, ApJ, 509, 717.

Dall, T., Fynbo, J., Pedersen, H., Jensen, B., Hjorth, J., and Gorosabel, J. 2000, GCN notice 804.

DiPaola, A. et al. 2000, GCN notice 816.

Frail, D. A. et al. 2000, ApJ, 538, L129.

Fynbo, J. P. U., Moller, P., Dall, T., Pedersen, H., Jensen, B. L., Hjorth, J., and Gorosabel, J. 2000, GCN notice 825.

Fynbo, J. U. et al. 2001, A&A submitted. Astro-ph 0102158.

Galama, T. J. et al. 2001, in preparation.

Garmire, G., Garmire, A., Piro, L., and Garcia, M. R. 2000, GCN notice 836.

Gorosabel, J., Ceron, J. M. C., Castro-Tirado, A., and Greiner, J. 2000, GCN notice 803.

Granot, J., Piran, T., and Sari, R. 1999a, ApJ, 513, 679.

Granot, J., Piran, T., and Sari, R. 1999b, ApJ, 527, 236.

Holtzman, J. A., Burrows, C. J., Casertano, S., Hester, J. J., Trauger, J. T., Watson, A. M., and Worthey, G. 1995, PASP, 107, 1065.

Hurley, K., Mazets, E., Golenetskii, S., and Cline, T. 2000, GCN notice 802.

Kobayashi, S. and Sari, R. 2001, ApJ, in press (astro-ph/0101006).

Kulkarni, S. R. *et al.* 1999, ApJ, 522, L97.

Morrison, R. and McCammon, D. 1983, ApJ, 270, 119.

Panaitescu, A. and Kumar, P. 2000, ApJ, 543, 66.

Piro, L. *et al.* 2000, GCN 812.

Piro, L. *et al.* 2001, In preparation.

Price, P. A. et al. 2001, ApJ Letters, in press.

Sari, R. 1997, ApJ, 489, L37.

Sari, R. and Esin, E. 2001, ApJ, 548, 787.

Sari, R., Piran, T., and Halpern, J. P. 1999, ApJ, 519, L17.

Sari, R., Piran, T., and Narayan, R. 1998, ApJ, 497, L17.

Schlegel, D. J., Finkbeiner, D. P., and Davis, M. 1998, ApJ, 500, 525.

Wainscoat, R. J. and Cowie, L. L. 1992, AJ, 103, 332.